Research Article

Effect of Ti additions on microstructure and mechanical properties of Cu–Cr–Zr alloy

Chenying Shi [a], Muzhi Ma [b], Biaobiao Yang [a,c,d], Yuling Liu [a,*], Yushen Huang [a], Yong Du [a,*]

[a] *State Key Laboratory of Powder Metallurgy, Central South University, Changsha 410083, China*
[b] *School of Materials Science and Engineering, Central South University, Changsha 410083, China*
[c] *IMDEA Materials Institute, C/Eric Kandel 2, Getafe, 28906 Madrid, Spain*
[d] *Department of Materials Science, Polytechnic University of Madrid/Universidad Politécnica de Madrid, E.T.S. de Ingenieros de Caminos, 28040 Madrid, Spain*

A B S T R A C T

Ti additions in Cu–Cr–Zr alloys are useful for achieving high mechanical properties. In this work, the influence of Ti contents (0.25 wt%, 0.6 wt%, and 1.02 wt%) on the microstructure, mechanical, and electrical properties of Cu–Cr–Zr alloys has been investigated experimentally, along with thermodynamic and kinetic calculations. The electrical conductivity decreased but the hardness/strength increased with increasing Ti content. The lower electrical conductivity is due to increased electron scattering through the solution of more Ti atoms in the Cu matrix. As for the higher hardness/strength, it is mainly owing to higher dislocation density and finer FCC-Cr precipitates. Furthermore, a model considering the size distributions of precipitates is adopted to calculate precipitation strengthening quantitatively. The calculated yield strengths are consistent with the experimental ones for the alloys. The thermodynamic and kinetic calculations reveal that increasing Ti content can facilitate the nucleation of FCC-Cr but enhance its activation energy, hence hindering the growth process. The present work study can provide an effective strategy for producing copper alloys with expected performance.

© 2023 Published by Elsevier Ltd on behalf of The editorial office of Journal of Materials Science & Technology.

1. Introduction

Cu–Cr–Zr alloys are extensively used as industrial components like lead frame materials, electric/microelectronics, nuclear reactors, etc., due to their good thermal/electrical conductivity, high performance-price ratio, and outstanding mechanical properties [1–5]. Such superior mechanical properties, especially high strength, are closely bound up with low solubility of Cr/Zr in Cu and the dispersion of secondary particles in the matrix [6,7]. To the best of our knowledge, the most common-used and effective strategy to prepare high-strength Cu–Cr–Zr alloys is the combination of severe deformation such as cold rolling and subsequent aging treatment (mostly at low aging temperatures). Severe deformation refines grains and generates amounts of dislocations, and subsequent aging treatment enables the formation of dispersed precipitates and relaxation of partial internal stress being available [8,9].

To meet the ever-growing demands of high-performance alloys for industry, the preparation and design of novel Cu–Cr–Zr alloys

have been attracting considerable attention from researchers [10–16]. Main strengthening strategies can be categorized as composite reinforcement [11], alloying with other elements like Nb [10], Ag [14], Ti [16], rare earth [12], and thermo-mechanical process parameters optimization [13,15]. Among them, the alloying of Ti has been demonstrated to improve the mechanical property of Cu–Cr–Zr alloys remarkably, at the expense of the slightly increased cost of their production [16–25]. For example, Krishna et al. [17–21] and Kumar et al. [22] reported that the trace addition of Ti can promote grain refinement and improve the mechanical strength of Cu–Cr–Zr alloys. Moreover, Krishna et al. [23] further found that a small addition of Ti can prevent sulfur embrittlement. In the study of Rao et al. [24], the high strength of Cu–Cr–Zr–Ti alloy was mainly attributed to the fine Cr-rich precipitates. Wang et al. [25] determined the location of the Cr, Zr, and Ti atoms in the Cr-rich precipitates by atom probe tomography (APT) observation, and they reached the following conclusions: (a) the presence of Ti can decrease the nucleation barrier for the FCC-Cr nuclei; (b) the vast number of fine coherent FCC Cr-rich precipitates should account for high strength of Cu–Cr–Zr–Ti alloys. Despite the above studies, the correlation among Ti content, microstructure, and mechanical properties of Cu–Cr–Zr alloys is still not thoroughly understood.

---

* Corresponding authors.
E-mail addresses: liu.yuling@csu.edu.cn (Y. Liu), yong-du@csu.edu.cn (Y. Du).

Table 1
Actual compositions of the alloys measured via ICP-OES (wt.%).

Alloys	Cr	Zr	Ti	Cu
0.25Ti	0.24	0.11	0.25	99.40
0.6Ti	0.24	0.12	0.6	99.04
1.02Ti	0.21	0.13	1.02	98.64

Specifically, previous works on Cu–Cr–Zr–Ti alloys were unfortunately limited to low and individual Ti compositions. How alloying of high Ti contents to Cu–Cr–Zr alloys influences their microstructure and mechanical properties still needs systematic experimental and theoretical investigations.

The aim of the present study is thus to figure out the influence of Ti additions (0.25 wt%, 0.6 wt%, and 1.02 wt%) on the microstructure and mechanical properties of Cu–Cr–Zr alloy. The strengthening mechanisms for the high strength of Cu–Cr–Zr–Ti alloys are quantitatively calculated, and the influence of various Ti contents on different strengthening parts is also explored. Furthermore, the nucleation and growth mechanisms of Cr precipitates in Cu–Cr–Zr–Ti alloys are systematically discussed according to the thermodynamic and kinetic analysis.

2. Experimental procedure

High-purity Cu (99.99 wt%), Cr (99.95 wt.%), Zr (99.9 wt%), and Ti (99.9 wt%) were used as starting materials. Based on these pure metals, Cu–10Cr, Cu–13Zr, and Cu–20Ti (wt%) master alloys were first prepared. Subsequently, Cu–Cr–Zr–Ti alloys with nominal compositions of Cu–0.22Cr–0.12Zr–xTi (x = 0.25 wt%, 0.6 wt%, and 1 wt%) were prepared with high-purity Cu and these master alloys by medium frequency induction furnace. The mixture of graphite powder and crushed charcoal was used as the covering agent to prevent melt oxidation. The obtained ingots were cut into cubes (30 mm × 30 mm × 10 mm) using electrical discharge machining (EDM, DK7735, Taizhou XeoFon Machine Co., Ltd., Taizhou, China). They were solid solution annealed (SSA) at 950 °C for 1 h, followed by water quenching. The actual chemical compositions of the ingots were measured by Inductively Coupled Plasma Optical Emission Spectrometer (ICP-OES, Spectro Blue, Spectro Analytical Instruments GmbH, Kleve, Germany), as shown in Table 1. Based on it, the Cu–Cr–Zr–xTi (x = 0.25 wt%, 0.6 wt%, and 1.02 wt%) alloys (aging treatment: 450 °C + 2 h) are named as 0.25Ti, 0.6Ti, and 1.02Ti alloys, respectively and hereafter in this work. Then the SSA ingots were further cold rolled (CR) from 10 to 2 mm in thickness with a reduction of 80%. Finally, after CR treatment, the samples were subjected to aging treatment at 450 °C for different duration times.

Two sets of three different alloys were subjected to aging treatments ranging from 0 to 36 h, followed by hardness and electrical conductivity tests after each annealing cycle. Hardness tests were carried out on a Vickers hardness tester (MicroMet-5104, Buehler, Lake Bluff, USA) under a 3.0 kg load for 10 s, and each sample was measured 8 times to guarantee repeatability. Electrical conductivities were measured on a conductivity meter (D60K, Xiamen XinBoTe Technology Co., Ltd., Xiamen, China), and the average value and the standard deviation of 5 measurements were taken with the unit of international annealed copper standard (IACS).

Furthermore, tensile tests and microstructural characterization were performed on the peak-aged alloys (aging treatment: 450 °C + 2 h). Four tensile measurements were conducted for each sample, using a universal material testing machine (UTM5105, Shandong OBT Test Equipment Co., Ltd., Shandong, China) under

a strain rate of 0.5 mm min^{-1}. The microstructural characterization of the peak-aged alloys was conducted using an optical microscope (OM, DM4M, Leica, Wetzlar, Germany), field-emission scanning electron microscope (SEM, FEI Quanta 650, FEI, Hillsboro, USA) equipped with electron backscattered diffraction (EBSD, Oxford HKL Channel 5, Oxford Instruments, Abingdon, UK; step size: 1.5 μm), and field-emission transmission electron microscope (TEM, FEI Tecnai G2 F20, FEI, Hillsboro, USA). Noted that samples for OM and EBSD were all mechanically ground using SiC paper (up to 2000 grit), and polished with the 0.3 μm Al$_2$O$_3$ suspension solution. Then, the samples for OM observation were finally etched in the mixture solution of 5 g FeCl$_3$ + 50 mL HCl + 100 mL CH$_3$CH$_2$OH at room temperature, while the samples for EBSD were further polished using a suspension containing oxide particles of 40 nm. As for the samples for TEM analysis, they were twin-jet electrolytic-polished in the mixture solution of CH$_3$OH:HNO$_3$ = 3:1 (volume ratio) under the conditions of the temperature and voltage of –30 °C and 12 V, respectively. The X-Ray diffraction (XRD) method was also utilized to determine phase composition and structural peculiarity of the obtained samples using the X-ray diffractometer (XRD, Bruker-AXS D8, Bruker, Germany) equipped with Cu-Kα radiation source. The scanning rate was chosen to be 0.02° s^{-1}, the 2θ range was 30°–100°, as well as the step size was assigned to 0.01°.

3. Experimental results and discussion

3.1. Electrical conductivity and mechanical properties

Fig. 1 displays the variations of both hardness and electrical conductivity of the Cu–Cr–Zr–xTi alloys aged at 450 °C for different annealing times. As shown in Fig. 1(a), the same variation tendency is found for all alloys. To be specific, the hardness increased first, and gradually reached the peak hardness after 2 h annealing, then decreased with aging time further prolonging. Besides that, a distinct and positive correlation between Ti content and hardness value is observed. The peak-aged hardness values of 0.25Ti, 0.6Ti, and 1.02Ti alloys are 203 ± 5, 218 ± 2, and 238 ± 5 HV, respectively (Table 2). Meanwhile, Ti content shows a weak impact on the variation tendency of electrical conductivity, whilst exhibiting a strong yet negative correlation with the value of electrical conductivity (Fig. 1(b)). Under the peak-aged state, with the content of Ti increasing from 0.25 wt% to 0.60 wt%, then to 1.02 wt%, the electrical conductivity of alloy drops from 41 ± 0.1 to 29 ± 0.1, then to 26 ± 0.1%IACS. This can be explained by the increased electron scattering through the solution of more Ti atoms in the Cu matrix under higher Ti alloying to Cu–Cr–Zr alloy. A similar effect of the added Ti on the electrical conductivity of Cu alloys was reported in Cu–Ti alloys [26,27] and Cu–Ni–Si–Ti alloys [28].
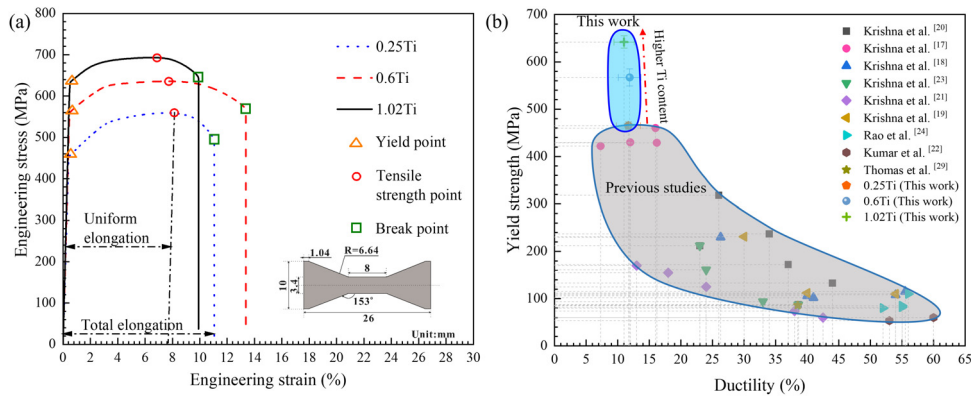
Fig. 2(a) shows the tensile engineering stress-strain curves of 0.25Ti, 0.6Ti, and 1.02Ti alloys. Higher Ti content is accompanied by higher yield and tensile strengths, whilst the elongation rate differs little with Ti content varying (Table 2). Ashby map of ductility versus yield strength for Cu–Cr–Zr–Ti alloys of this work and other previously reported literature [17–24,29] is plotted in Fig. 2(b). Note that the total tensile elongation of this work is used here as ductility value. Obviously, the yield strengths measured in this work are higher than the ones from previously studied Cu–Cr–Zr–Ti alloys. This could be attributed to large cold deformation (reduction rate: 80%) and higher contents of Ti used in this study. Furthermore, after tensile tests, the fracture morphology of all alloys is characterized by a mixture of dimples and cleavage planes, as well as no obvious necking is observed, indicating that all alloys suffer quasi-cleavage fracture, as shown in Fig. 3. The fracture
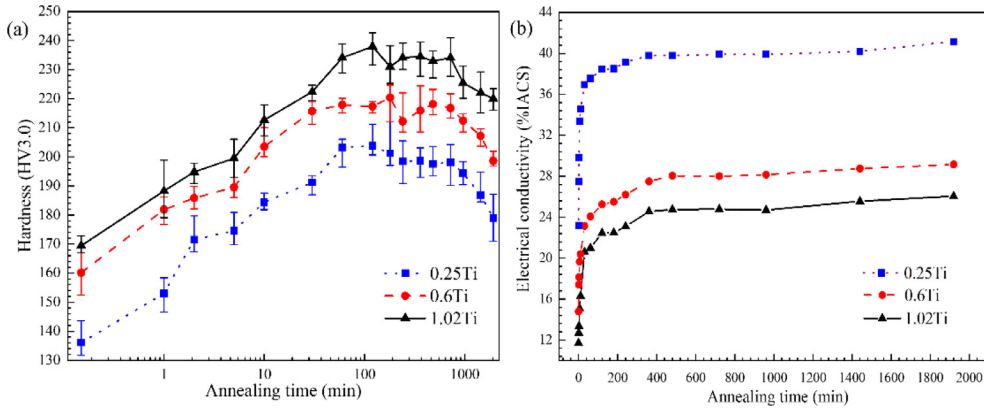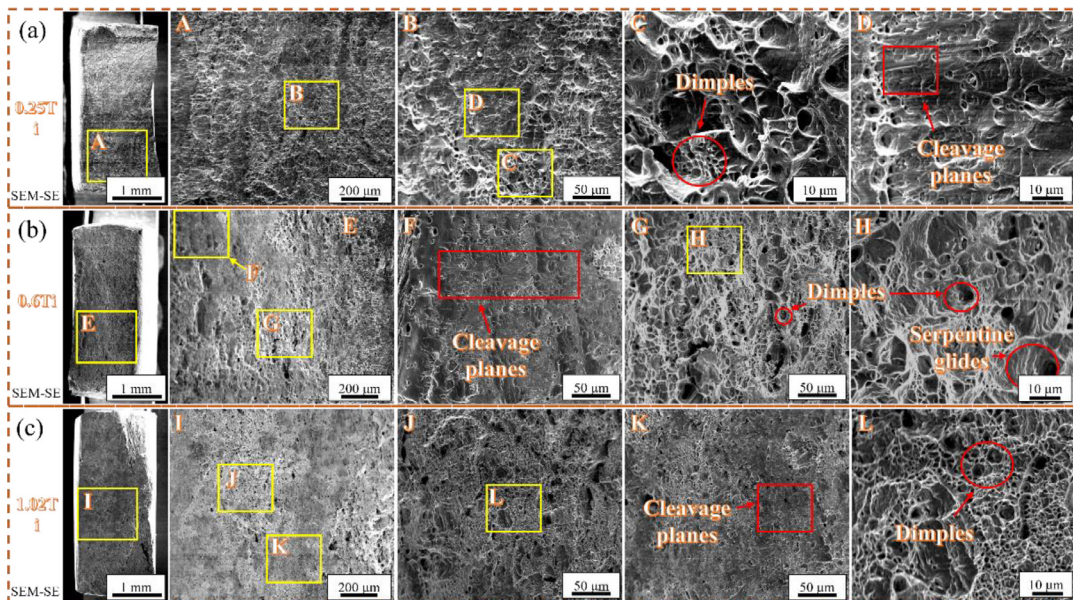
Fig. 1. Properties of 0.25Ti, 0.6Ti, and 1.02Ti alloys: the variations of (a) hardness and (b) electrical conductivity with aging time prolonging from 0 to 32 h. The aging temperature is 450 °C.

Table 2
Mechanical properties and electrical conductivities of 0.25Ti, 0.6Ti, and 1.02Ti alloys.

Alloys	Hardness (HV)	Conductivity (%IACS)	Yield strength (MPa)	Tensile strength (MPa)	Uniform elongation (%)	Total elongation (%)
0.25Ti	203 ± 5	41 ± 0.1	465 ± 8	559 ± 14	7.8 ± 0.3	11.7 ± 1.9
0.6Ti	218 ± 2	29 ± 0.1	567 ± 18	635 ± 22	7.6 ± 0.6	11.9 ± 1.8
1.02Ti	238 ± 5	26 ± 0.1	642 ± 13	694 ± 20	6.7 ± 0.5	11.0 ± 1.6

Fig. 2. (a) Tensile engineering stress–strain curves of 0.25Ti, 0.6Ti, and 1.02Ti alloys, (b) Ashby diagram of the yield strength and ductility of this work and these of literature [17–24,29].

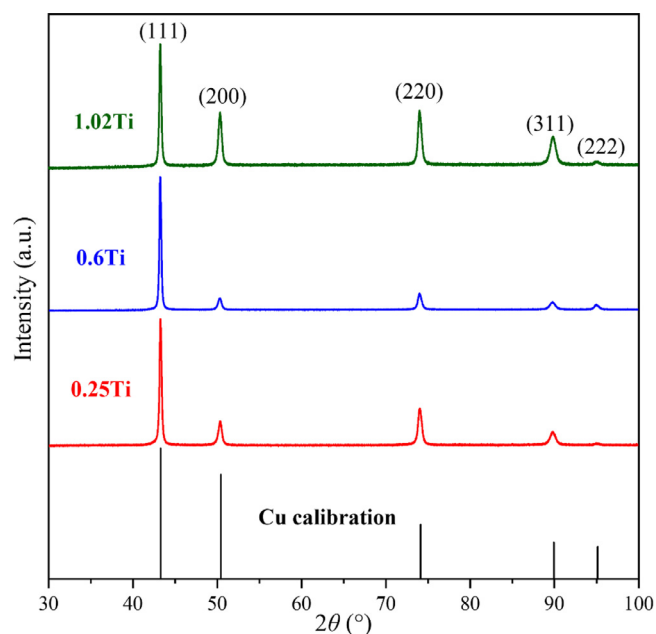**Fig. 3.** Fracture morphologies of (a) 0.25Ti, (b) 0.6Ti, and (c) 1.02Ti alloys.

Fig. 4. XRD patterns of the 0.25Ti, 0.6Ti, and 1.02Ti alloys.

Table 3
Summary of XRD peak positions for 0.25Ti, 0.6Ti, and 1.02Ti alloys (°).

Alloys	Peak 1/2θ	Peak 2/2θ	Peak 3/2θ	Peak 4/2θ	Peak 5/2θ
0.25Ti	43.3146	50.3780	74.0882	89.8851	95.0718
0.6Ti	43.3032	50.3575	74.0826	89.8413	95.0283
1.02Ti	43.2819	50.3444	74.0718	89.8280	94.9931

morphology of the dimples may reflect the plasticity of the alloy to some extent. To be specific, the formation and growth of dimples can absorb plastic strain energy generated during the deformation, thereby the higher dimple size/depth generally accompanies the higher tensile ductility [30–32]. The dimples in 1.02Ti (Fig. 3(c)) are slightly shallower and smaller than those in 0.25Ti (Fig. 3(a)) and 0.6Ti (Fig. 3(b)), indicating the plasticity in the alloy 1.02Ti is probably inferior to that of the alloy 0.25Ti or 0.6Ti. And this observation is consistent with the experimental results presented in Table 2, i.e., the total elongation for 1.02Ti (11.0% ± 1.6%) is slightly lower compared to that of 0.2Ti (11.9% ± 1.8%) and 0.6Ti (11.7% ± 1.9%).

3.2. Microstructural evolution

Fig. 4 presents the XRD patterns of 0.25Ti, 0.6Ti, and 1.02Ti alloys, along with the XRD pattern from PDF card #04-0836 (Cu). Only the Cu matrix is detected in Fig. 4, while the presence or absence of precipitates still needs further characterization, given the resolution limitation of XRD. Table 3 lists the diffraction peak positions for the three alloys. And the diffraction peak positions gradually shift to the left with increasing Ti content. This is presumably related to higher Ti contents resulting from more Ti atoms (atomic radius: 0.147 nm) substitutions for Cu (atomic radius: 0.128 nm) unit cell, causing the increase of lattice parameters.

Fig. 5 shows the optical micrographs of 0.25Ti, 0.6Ti, and 1.02Ti alloys. Large pancake-shaped elongated grains along the rolling direction and small recrystallized grains are observed. Noted that the serrated boundary characteristic of the elongated grains is also characterized by EBSD (Fig. S1 in the Supplementary Information), and can be explained well as the manifestation of strain-induced boundary migration [16,33].

In order to image the fine-scale features within the grains, a higher-resolution analysis was conducted using TEM. Fig. 6 shows the TEM images of 0.25Ti alloy. In Fig. 6(a, b), high-density dislocation networks and dislocation tangles, as well as spherical and coffee-bean precipitates, are clearly observed. The large cold deformation before aging treatment can greatly increase the number of defects, such as dislocation networks and dislocation tangles, which are generally recognized as high-energy configurations and thus reasonably acts as heterogeneous nuclei during the subsequent aging process [34–36]. The selected area electron diffraction (SAED) pattern in Fig. 6(c) demonstrates the existence of the FCC-Cu matrix and FCC-Cr precipitate, and their cube-on-cube orientation relationship (OR). The Moiré fringes are also observed (Fig. 6(d)), owing to the interference between Cu and Cr reflections. The high-resolution transmission electron microscope (HRTEM) (Fig. 6(e)) and the corresponding fast Fourier transform (FFT) images (Fig. 6(f)) further verify the presence of FCC-Cr precipitate, and also its cube-on-cube OR with the Cu matrix. Akin to 0.25Ti alloy, dislocation-tangles, spherical and coffee-bean precipitates as well as Moiré fringes patterns are also observed in the TEM micrographs of 0.6Ti (Fig. 7) and 1.02Ti (Fig. 8) alloys. However, different SAED and FFT patterns are observed in these two alloys. To be specific, in 0.6Ti alloy, no diffraction pattern of precipitate is found in the SAED image (Fig. 7(b)) and FFT (Fig. 7(e)). Further inverse fast Fourier transform (IFFT) image shown in Fig. 7(f) demonstrates a fully coherent interface between the precipitates and the matrix. And the fully coherent precipitates are recognized as FCC-Cr, as reported by other previous studies [25,37]. Besides, in 1.02Ti alloy, only the diffraction pattern of matrix FCC-Cu is observed in the SAED image (Fig. 8(c)), whilst in addition to FCC-Cr, the presence of β'-Cu$_4$Ti precipitate is identified from the HRTEM (Fig. 8(e)) and the corresponding FFT (Fig. 8(f)) images. The crystal OR between the Cu matrix and β'-Cu$_4$Ti precipitate is determined to be $[\bar{1}12]_{Cu}$ // $[011]_{\beta'\text{-Cu4Ti}}$. Note that β'-Cu$_4$Ti precipitate is a metastable phase and coherent with matrix Cu through spinodal decomposition [38,39]. Such a coherent characteristic is also verified in the IFFT image (Fig. 8(i)). The precipitate size distributions of 0.25Ti, 0.6Ti, and 1.02Ti alloys are presented in Fig. 9. Note that the precipitate size was collected from HRTEM images using Nano Measurer 1.2 software. The peak value of precipitate diameter is determined as 1.33, 1.30, and 1.28 nm for 0.25Ti, 0.6Ti, and 1.02Ti, respectively. The average precipitate diameters are also determined as 2.02 (0.25Ti), 1.79 (0.6Ti), and 2.10 (1.02Ti) nm. These TEM results demonstrate that the nucleation and growth behaviors of precipitates in Cu–Cr–Zr–Ti alloy are probably different in 0.25Ti, 0.6Ti, and 1.02Ti alloys.

4. Calculated results and discussion

4.1. Effect of Ti on the strengthening mechanism

The yield strength of the alloy is usually defined by four strengthening mechanisms:

$$\sigma_{total} = \sigma_0 + \Delta\sigma_d + \Delta\sigma_{ss} + \Delta\sigma_{gbs} + \Delta\sigma_p \tag{1}$$

where σ_{total} is the yield strength of the alloy, σ_0 is the intrinsic lattice stress of the copper matrix ($\sigma_0 = 40$ MPa [40]), $\Delta\sigma_d$ is the dislocation strengthening, $\Delta\sigma_{ss}$ is the solid solution strengthening, $\Delta\sigma_{gbs}$ is the grain boundary strengthening, and $\Delta\sigma_p$ is the precipitation strengthening.

4.1.1. Dislocation strengthening
The dislocation strengthening, $\Delta\sigma_d$, can be estimated by the Taylor relation [41]:

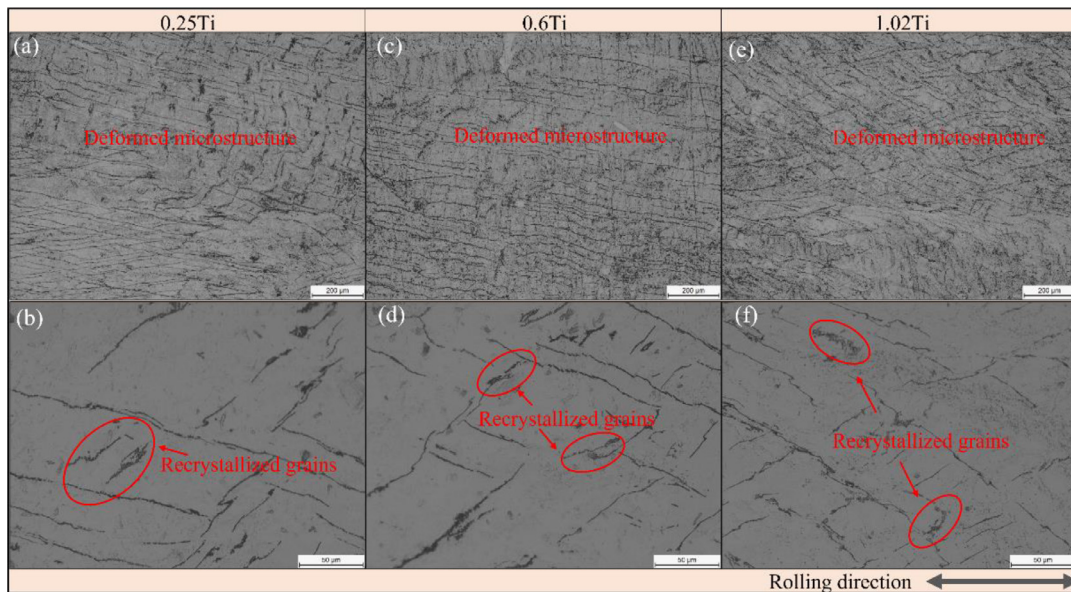$$\Delta\sigma_d = M\alpha Gb\rho^{\frac{1}{2}} \tag{2}$$

Fig. 5. Metallographic microstructure under peak-aged state: (a, b) 0.25Ti, (c, d) 0.6Ti, and (e, f) 1.02Ti alloys.

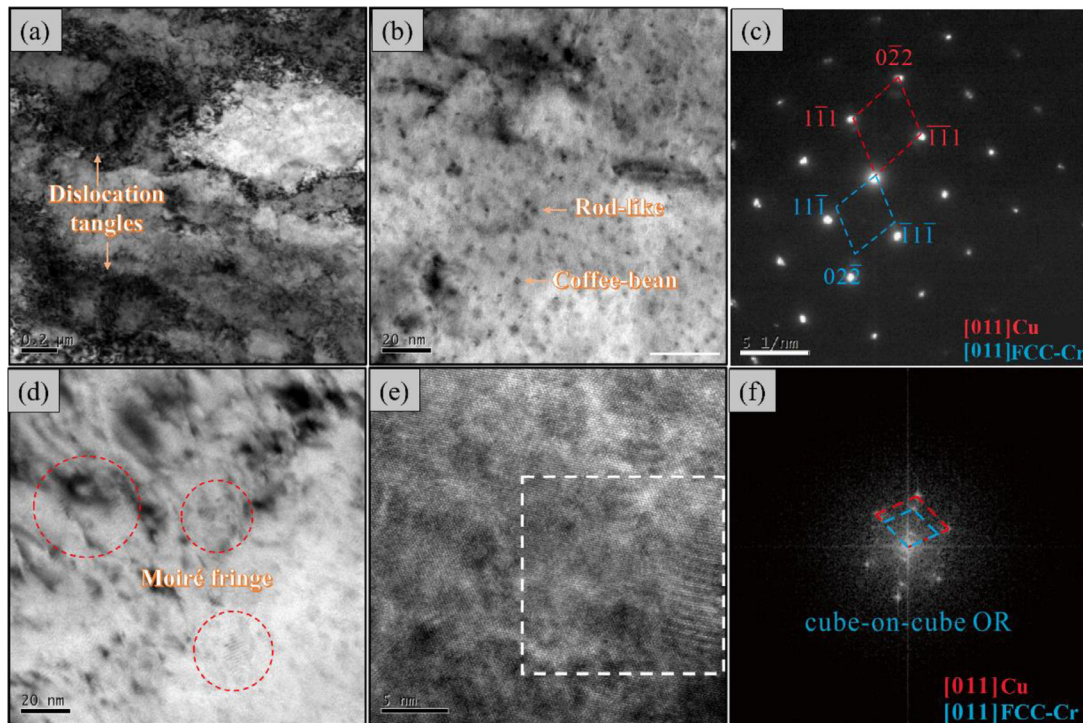**Fig. 6.** TEM images of the 0.25Ti alloy: (a, b, d) bright-field images, (c) SAED viewed along the zone axis of $[011]_{Cu}$, (e) HRTEM images, and (f) corresponding FFT patterns.

where M is the Taylor factor of the Cu matrix with a value of 3.06 [42], α is a constant parameter ($\alpha = 0.2$ [43]), G is the shear modulus of the Cu matrix with a value of 45.5 GPa [44], b is the Burgers vector of Cu matrix with a value of 0.2556 nm [44]. ρ is the dislocation density measured by the following equation [45]:

$$\rho = \frac{16.1\varepsilon^2}{b^2} \tag{3}$$

where ε is the microstrain obtained from XRD results using the Williamson-Hall plot method [46].

4.1.2. Solid solution strengthening

The solid solution strengthening, $\Delta\sigma_{ss}$, can be expressed as the following formula [47]:

$$\Delta\sigma_{ss} = \sum MG\frac{\epsilon_{ss}^{\frac{3}{2}}c^{\frac{1}{2}}}{700} \tag{4}$$

where ϵ_{ss} is the misfit strain due to a lattice distortion near solute, herein taken as 0.015, 0.11, and 1.97 for Cr [48], Zr [49], and Ti [50], respectively; c is the mass percent of solute atoms in the Cu matrix. Based on the thermodynamic parameters of the Cu–Cr–Zr [51], and Cu–Zr–Ti [52] ternary systems, the thermodynamic description of the Cu–Cr–Zr–Ti quaternary system was extrapolated using the
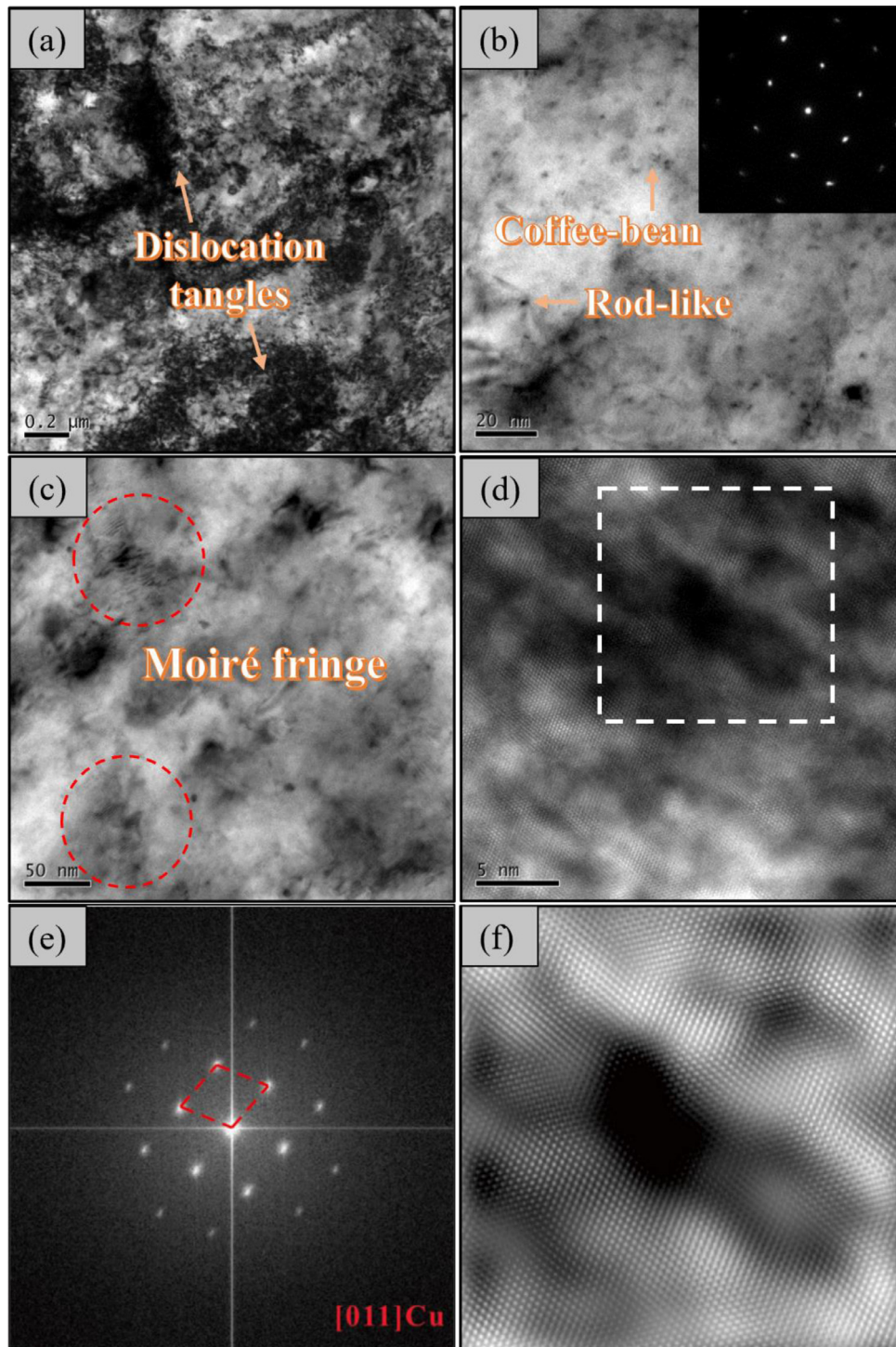
Fig. 7. TEM images of the 0.6Ti alloy: (a, b, c) bright-field images, SAED viewed along the zone axis of $[011]_{Cu}$, (d) HRTEM images, (e) corresponding FFT patterns, and (f) corresponding IFFT patterns.

Redlich-Kister-Muggianu model [53,54]. The mass percent of solute atoms after 450 °C aging treatment, c, was evaluated by the CALculation of the PHAse Diagram (CALPHAD) method.

4.1.3. Grain boundary strengthening

The grain boundary strengthening, $\Delta\sigma_{gbs}$, can be expressed using the Hall-Petch formula [55,56]:

$$\Delta\sigma_{gbs} = \frac{k}{\sqrt{d}} \qquad (5)$$

where k is a constant of the Cu alloys ($k = 0.14$ MPa $\cdot \sqrt{m}$ [57]), and d is the average diameter of the grain. Note that the indexing of EBSD is not high enough ($\sim$65%) to give accurate grain size statistics from the perspective of authors (Fig. S1), thus d is estimated from metallographic microstructure (Fig. 5) using the conventional intercept method [58].

4.1.4. Precipitation strengthening

Previous estimations [17,20,23] on precipitation strengthening contributions for Cu–Cr–Zr–Ti alloys only consider either dislo-
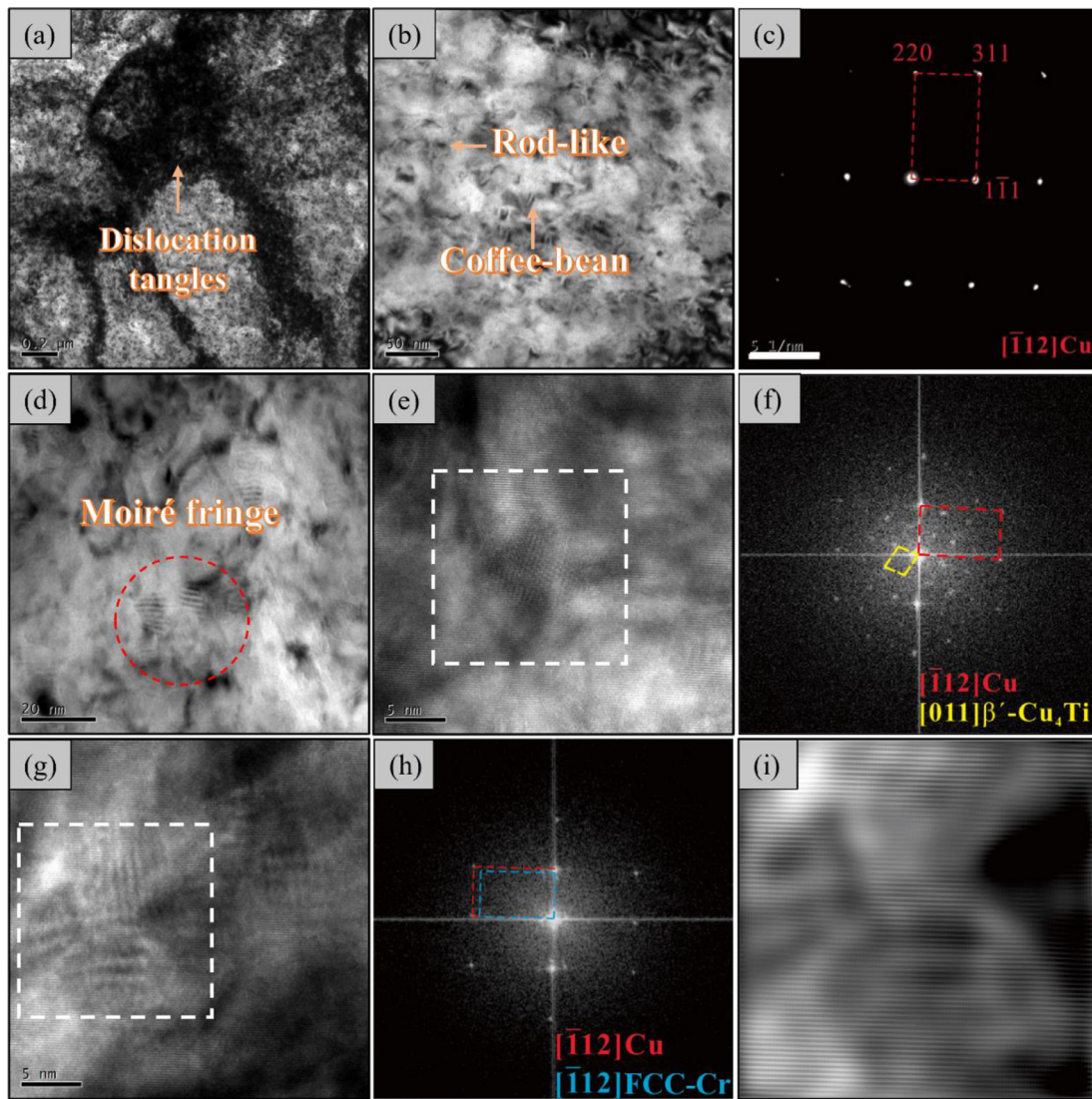
Fig. 8. TEM images of the 1.02Ti alloy: (a, b, d) bright-field images, (c) SAED viewed along the zone axis of $[\bar{1}12]_{Cu}$, (e, g) HRTEM images, (f, h) corresponding FFT patterns, and (i) corresponding IFFT patterns.
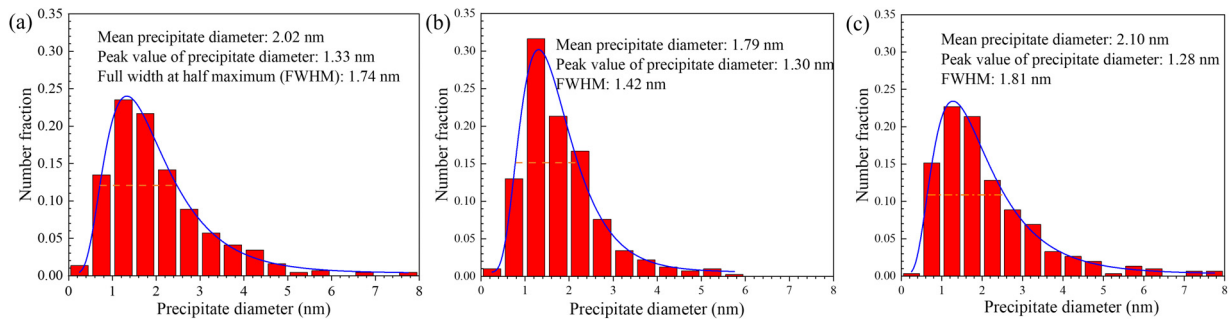
Fig. 9. Precipitates size distribution statistics: (a) 0.25Ti, (b) 0.6Ti, and (c) 1.02Ti alloys. Note FWHM is the abbreviation of Full width at half maximum.

cation shearing or bypassing mechanisms, but not both. One of the novelties of this work is to adopt a strengthening model for particles, which considers the size distributions of precipitates. Therefore, the contribution of precipitation strengthening to yield strength can be evaluated comprehensively. The precipitates are simplified to be spherical particles, and the precipitation strength-

ening ($\Delta\sigma_p$) can be expressed as follows [59]:

$$\Delta\sigma_p = 0.9MGb\sqrt{N}\,\bar{F}^{\frac{3}{2}}\left(1 - \frac{1}{6}\bar{F}^5\right) \qquad (6)$$

where N is the density of obstacles per area on the slip plane; $\bar{F}$ is the average value of the obstacle strengths of the particles. N is

Table 4

Calculated contributions of the dislocation strengthening, solid solution strengthening, grain boundary strengthening, and precipitation strengthening on the yield strengths of alloys.

Alloys	ε	ρ (m^{-2})	$\Delta\sigma_d$ (MPa)	c_{Cr} (wt.%)	c_{Zr} (wt.%)	c_{Ti} (wt.%)	$\Delta\sigma_{ss}$ (MPa)	d (μm)	$\Delta\sigma_{gbs}$ (MPa)	$\bar{r}$ (nm)	f_v (%)	N_V (m^{-3})	$\bar{F}$	$\Delta\sigma_p$ (MPa)
0.25Ti	0.00164	6.6281×10^{14}	183.2	0.00369	0.00285	0.250	27.5	10.54	43.1	1.01	0.60	5.284×10^{23}	0.3294	168.2
0.6Ti	0.00259	1.6531×10^{15}	289.4	0.00361	0.00279	0.263	28.2	9.91	44.5	0.90	0.68	1.142×10^{24}	0.2638	162.1
1.02Ti	0.00332	2.7163×10^{15}	370.9	0.00345	0.00230	0.262	28.2	11.14	41.9	1.05	0.88	6.457×10^{23}	0.3267	221.2
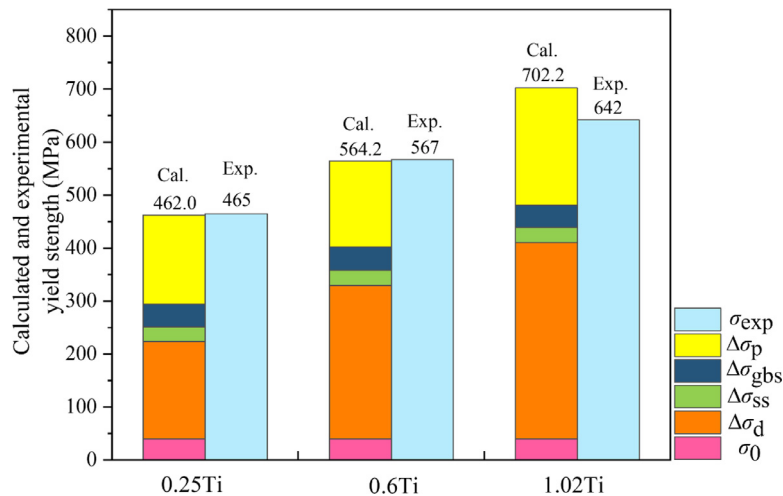
Fig. 10. Calculated and experimental yield strengths of 0.25Ti, 0.6Ti, and 1.02Ti alloys.

expressed by the following equation [59]:

$$N = 2 \int_0^\infty r\phi_r \mathrm{d}r = 2\bar{r}N_V \qquad (7)$$

where r and $\bar{r}$ are the radius of the precipitate particle and the mean radius of the particles, respectively; N_V is the number density of precipitates (in particles per m^3); ϕ_r is the statistical distribution of the number of particles per volume, which meets the formula $\int_0^\infty \phi_r \mathrm{d}r = N_V$. $\bar{r}$ can be estimated from the TEM images.

The mean of the obstacle strengths of the particles ($\bar{F}$) can be defined by the following equation [59]:

$$\bar{F} = \left(\frac{1}{r_c^{2\kappa}} \int_0^{r_c} r^{2\kappa+1}\phi_r \mathrm{d}r + \int_{r_c}^\infty r\phi_r \mathrm{d}r \right) \frac{1}{\bar{r}N_V} \qquad (8)$$

where r_c is the maximal radius of particles that the dislocation can cut; N_V is the number density of precipitates (in particles per m^3); κ is an empirical model parameter ($\kappa = 1$ [59]). r_c is estimated at 2 nm for precipitates in this work.

The statistical distribution of the number of particles (ϕ_r) can be fitted by the discrete equation as follows [60]:

$$\phi_r = \frac{N_V}{\sqrt{2\pi}sr} \exp\left(-\frac{1}{2s^2}\left(\ln\frac{r}{\bar{r}} + \frac{s^2}{2} \right)^2 \right) \qquad (9)$$

where s is the dispersion parameter and is estimated based on the discrete curve in Fig. 9. The values of s are fitted as 0.22, 0.21, and 0.24 for 0.25Ti, 0.6Ti, and 1.02Ti, respectively.

As for the number density of precipitates (N_V), it can be expressed as follows:

$$N_V = f_v \frac{V_0}{\int_0^\infty f_r \frac{4}{3}\pi (r)^3 \mathrm{d}r} \qquad (10)$$

where f_v is the volume fraction of precipitates as estimated from TEM images; V_0 is the unit volume ($V_0 = 1$ m^3); f_r is the proportion of the precipitates with radius r, and it can be assessed from the discrete curve in Fig. 9.

The corresponding results are summarized in Table 4. Therefore, the total yield strength σ_{total} of the alloys can be estimated from Eq. (1). Fig. 10 shows the comparison between calculated and experimental yield strengths. Considering the small proportion ($\leq$ 6%) of grain boundary strengthening in the total calculated yield strengths, some errors of the mean grain diameters in Eq. (5) have little influence on the overall statistics. In addition, the mean grain diameters can also be estimated from the average dislocation cell size using TEM images. Table 4 and Fig. 10 reveal that the calculated yield strengths of 0.25Ti and 0.6Ti are well consistent with the experimental ones, with deviations of 3 and 2.8 MPa, respectively. However, the calculated yield strength of 1.02Ti is higher than the experimental one with a deviation of 60.2 MPa. The main reason could be attributed that 1.02Ti has β'-Cu$_4$Ti precipitate in addition to FCC-Cr precipitate compared with 0.25Ti and 0.6Ti. The β'-Cu$_4$Ti phase has been reported to be formed via a spinodal decomposition involving clustering and ordering [38,39], which leads to a more complex strengthening mechanism and a larger statistical error. Despite that, with Ti content increasing, both calculated and experimental yield strengths are simultaneously increasing. To be specific, dislocation strengthening exhibits obvious and positive correlations with the alloying Ti content. Considering that all alloys were subjected to the same treatment, the increasing dislocation strengthening with Ti content increasing reveals that more dislocations should have been stored in the matrix for high Ti-bearing Cu–Cr–Zr alloy during cold deformation before aging. The dislocation and precipitation strengthening make major contributions to the increased yield strength according to this work. Such a finding is in accordance with the study by Krishna et al. [20] on Cu–0.5Cr–0.04Zr–0.03Ti (wt%) alloy after hot rolling at 500–800 °C. Compared with the study by Peng et al. [61], after the same 80% cold rolling and peak aging treatment, the precipitate strengthening of Cu-0.45Cr-0.28Ti (wt.%) alloy in Ref. [61] was 103.9 MPa, and that of 0.25Ti (Cu–0.24Cr–0.11Zr–0.25Ti (wt%)) alloy in this work was 168.2 MPa. It was reported that the higher Cr content should increase the precipitation strengthening [62]. On the other side, Tian
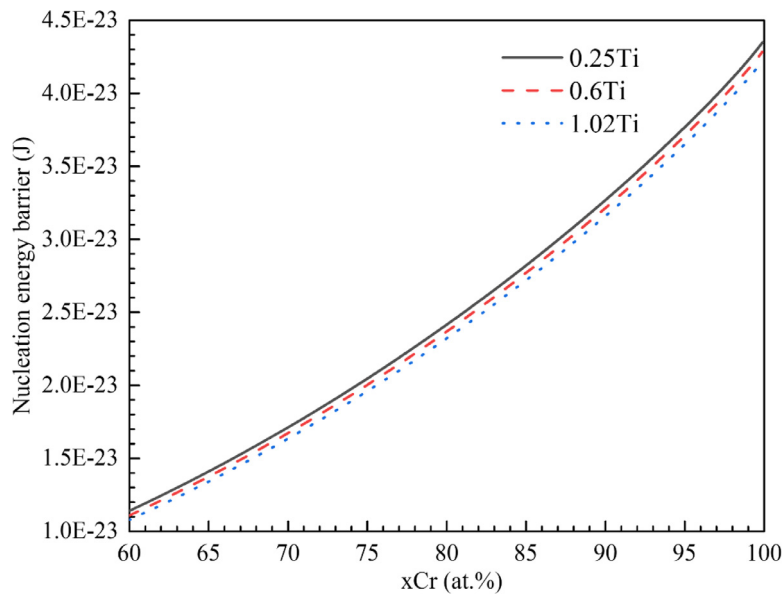
Fig. 11. Nucleation energy barrier of FCC-Cr precipitates in 0.25Ti, 0.6Ti, and 1.02Ti alloys.

et al. [63] reported that the addition of the Zr element can refine the Cr-rich precipitates and thus increase precipitation strengthening. These demonstrate that a higher precipitate strengthening in the alloy Cu–0.24Cr–0.11Zr–0.25Ti may be derived from a synergistic effect of Cr, Zr, and Ti alloying elements in Cu–Cr–Zr–Ti alloys.

4.2. Effect of ti on the precipitation behavior

As mentioned in Section 3.2, with Ti content increasing from 0.25 wt% to 1.02 wt%, the precipitate of the β'-Cu$_4$Ti phase is formed, with the volume fraction of precipitate particles increasing from 0.60% to 0.88% yet the slight variation of average precipitate diameter. This phenomenon should be closely related to the nucleation thermodynamic and growth kinetic of precipitates in Cu–Cr–Zr–Ti alloys. Thus their correlation with Ti content will be thoroughly discussed in the following sections.

4.2.1. The evolution of nucleation energy barrier

The nucleation energy barrier, ΔG^*, can be expressed as [64]:

$$\Delta G^* = g \frac{\gamma^3}{(\Delta G_v + \Delta G_e)^2} \tag{11}$$

where g is the geometry factor, γ is the interfacial energy, ΔG_v is the nucleation driving force per unit volume, and ΔG_e is the elastic strain energy.

The nucleation driving force per unit volume, ΔG_v, can be expressed as:

$$\Delta G_v = \Delta G_m / V_{mol} \tag{12}$$

where ΔG_m is the molar nucleation driving force and estimated based on the thermodynamic parameters of Cu–Cr–Zr–Ti alloys by CALPHAD method; V_{mol} is the molar volume and is calculated based on the lattice parameters.

The coherent elastic strain energy of the FCC-Cr and β'-Cu$_4$Ti can be expressed as [65]:

$$\Delta G_e = \frac{E}{1 - \nu} \left(\frac{a_m - a_p}{a_m} \right)^2 (x_m - x_p)^2 \tag{13}$$

where E is the elastic modulus, herein taken as 130 [66] and 155 GPa [67] for FCC-Cr and β'-Cu$_4$Ti, respectively; ν is Poisson's

ratio, herein taken as 0.34 [68] and 0.32 [67] for FCC-Cr and β'-Cu$_4$Ti, respectively; a_m and a_p are the lattice parameters of matrix and precipitates, obtained from Ref. [25]; x_m and x_p are the atom fractions of solute (Cr, Zr, and Ti) in matrix and precipitates, respectively. Since BCC-Cr precipitates exhibit an N–W and K–S orientation relationship that minimized the elastic energy, and also no BCC-Cr precipitates are identified, herein for simplicity, the elastic energy for BCC-Cr precipitate is neglected in the following calculations [66].

The interfacial energy of the FCC-Cr precipitate can be expressed as [66]:

$$\gamma = \frac{\Omega}{N_A \cdot Z} \left(\frac{x_m - x_p}{a_m} \right)^2 \tag{14}$$

where Ω is the interaction parameter; N_A is the Avogadro constant with a value of 6.02×10^{23} mol^{-1}; Z is the coordination number and is accepted as 12 for the FCC structure. The interfacial energy of between β'-Cu$_4$Ti and (Cu), as well as BCC-Cr and (Cu), were accepted as 320 [69] and 625 mJ m^{-2} [70], respectively.

Fig. 11 displays the evolution of the nucleation energy barrier of FCC-Cr precipitate in 0.25Ti, 0.6Ti, and 1.02Ti alloys with Cr content in FCC-Cr varying. Obviously, under various Cr contents, the nucleation energy barrier of FCC-Cr always shows a negative correlation with Ti content. This is one of the reasons why the volume fraction of FCC-Cr precipitate of 0.6Ti increased compared to that of 0.25Ti (0.17% → 0.22%). As for 1.02Ti alloy, the observed precipitates were β'-Cu$_4$Ti and FCC-Cr. And the nucleation energy barriers of FCC-Cr, BCC-Cr, and β'-Cu$_4$Ti precipitates in Cu–Cr–Zr–Ti alloys are presented in Fig. 12. Distinctly, the nucleation energy barrier increases with the following phase sequence: FCC-Cr < β'-Cu$_4$Ti < BCC-Cr. Noted that the BCC-Cr is transformed from the FCC-Cr precipitate. And the nucleation energy barrier of β'-Cu$_4$Ti is lower than the energy change from FCC-Cr to BCC-Cr (the values range from 9.37×10^{-21} to 6.03×10^{-18} based on Fig. 12), indicating that the precipitate of β'-Cu$_4$Ti precedes that of BCC-Cr. This agrees well with the observed microstructures by TEM (Figs. 6–8). Besides, the nucleation energy barrier of FCC-Cr is gradually decreasing with Ti content increasing in Cu–Cr–Zr–Ti alloys, in line with the result of Fig. 11. And a similar role of Ti was also reported in the study regarding Cu–0.43Cr–0.39Zr (wt%) and Cu–0.31Cr–0.29Zr–0.15Ti (wt%) alloys by thermodynamic calculations from Wang et al. [25].
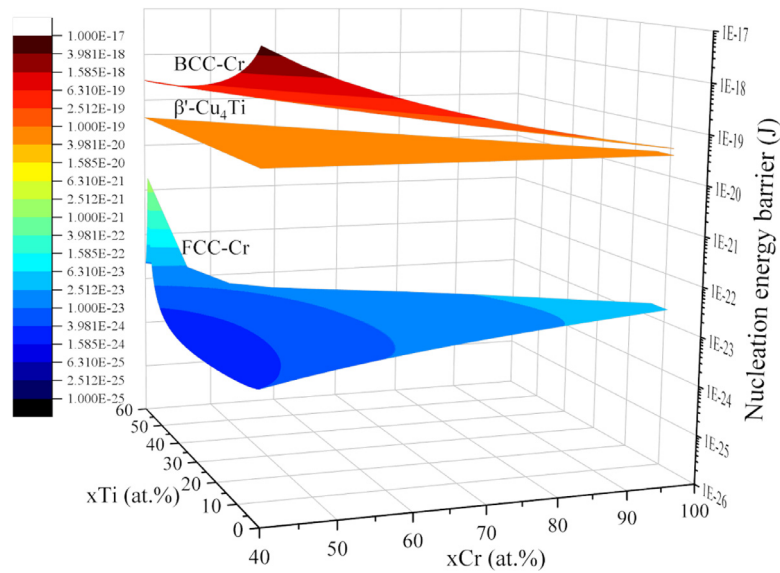
Fig. 12. Nucleation energy barrier of FCC-Cr, BCC-Cr, and β'-Cu$_4$Ti precipitates in Cu–Cr–Zr–Ti alloys.
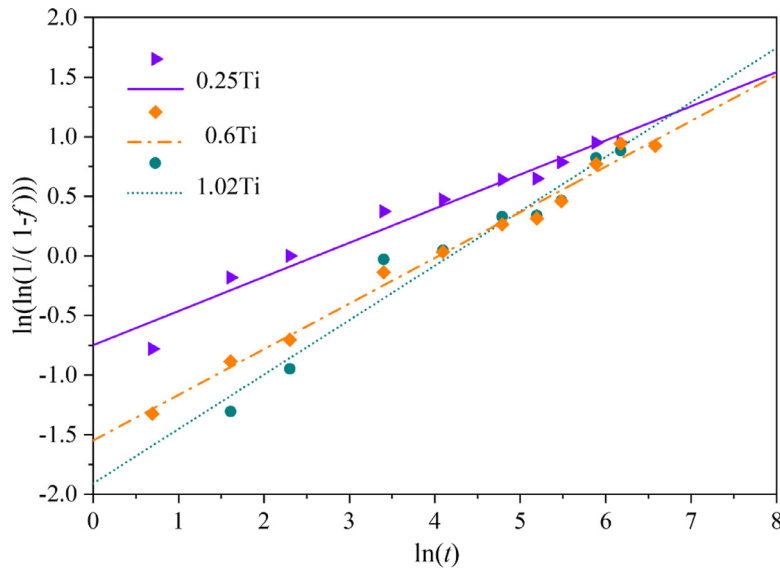

Fig. 13. $\ln[\ln(1/(1-f))]$–$\ln(t)$ curves of (a) 0.25Ti, (b) 0.6Ti, and (c) 1.02Ti alloys.

4.2.2. Precipitation growth kinetic during aging

The kinetic of precipitation growth can be assessed from the evolution of electrical conductivities of alloys. The fraction of phase transformation (f) can be described as:

$$f = V / V_1 \tag{15}$$

where V is the volume of new phases formed at a certain aging moment, V_1 is the equilibrium volume of new phases per unit volume of the matrix at the end of the precipitate (roughly 36 h in this work). The electrical conductivity (σ_e) of the alloy is proportional to the fraction of phase transformation [71]:

$$\sigma_e = \sigma_1 + (\sigma_{max} - \sigma_1) \cdot f \tag{16}$$

where σ_1 is the cold-rolling electrical conductivity before aging, σ_{max} is the maximum electrical conductivity in the later aging stage. f can be expressed based on the Avrami equations [72]:

$$f = 1 - \exp(-b \cdot t^n) \tag{17}$$

where b is a constant depending on the aging temperature, t is the aging time, and n is a constant depending on the phase transfor-

Table 5
Values of σ_1, σ_{max}, n, and $\ln(b)$ for 0.25Ti, 0.6Ti, and 1.02Ti alloys.

Alloys	σ_1 (MPa)	σ_{max} (MPa)	n	$\ln(b)$
0.25Ti	23.2	41.15	0.2865	−0.7489
0.6Ti	14.8	29.15	0.3832	−1.5493
1.02Ti	11.7	26.02	0.4570	−1.9093

mation mechanism and growth mechanism of the new precipitate phase. Eq. (17) can be converted as:

$$\ln\left(\ln\left(\frac{1}{1-f}\right)\right) = \ln(b) + n \cdot \ln(t) \tag{18}$$

Then $\ln(t)$ and $\ln(\ln(\frac{1}{1-f}))$ are selected as the abscissa and ordinate to plot the graph in Fig. 13, respectively. The slope of the line is the constant n, and the intercept is the $\ln(b)$. The values of σ_1, σ_{max}, n, and $\ln(b)$ of all alloys are listed in Table 5. b can be

expressed as [72]:

$$b = A \cdot \exp\left(-\frac{Q}{RT}\right) \tag{19}$$

where A is a constant, Q is activation energy during the precipitation growth, R is the gas constant, and T is aging temperature. Since all alloys undergo the same cold rolling and aging treatment with a slight difference in Ti content, parameter A can be taken as the same constant in these alloys. Then the activation energy Q can be qualitatively analyzed based on ln(b) in Table 5. The values of ln(b) are –0.7489, –1.5493, and –1.9093 for 0.25Ti, 0.6Ti, and 1.02Ti alloys, respectively. With Ti content increasing, the gradually decreasing ln(b) demonstrates the increasing activation energy, Q. This indicates the precipitates are harder to grow for higher Ti-bearing Cu-Cr-Zr alloys. This finding also supports the TEM investigations (Fig. 9): when there are only the FCC-Cr precipitates in the 0.25Ti and 0.6Ti alloys, the average size decreases from 2.02 to 1.79 nm with the increase of Ti content from 0.25 wt% to 0.6 wt%. Note that the increase of average size in 1.02Ti is presumably related to the incorporation of β'-Cu$_4$Ti, causing the precipitate growth behavior more complicated. Despite that, the fact of the larger activation energy in higher Ti content alloys explains the reason why it is hard to find the diffraction pattern of FCC-Cr precipitate in 0.6Ti and 1.02Ti alloys. The inhibitory effect of Ti on the growth of FCC-Cr precipitate was also reported in Cu–Cr–Ti alloys from studies of Zhang et al. [73] experimentally and Huang et al. [74] by calculations.

5. Conclusions

In this study, via the hybrid approach of mechanical tests, microstructural characterization as well as thermodynamic and kinetic analysis, the influence of various Ti contents (0.25 wt%, 0.6 wt%, and 1.02 wt%) on the microstructure and mechanical properties of Cu–Cr–Zr alloy has been systemically investigated. The main conclusions can be drawn as follows:

(1) The addition of Ti content is helpful to improve the hardness and yield strength of the Cu–Cr–Zr–Ti alloys, but this improvement is accompanied by a significant reduction in electrical conductivity.

(2) Dislocation strengthening through high-density dislocations and precipitation strengthening via FCC-Cr precipitates make main contributions to the yield strengths of the Cu–Cr–Zr–Ti alloys. Furthermore, with Ti concentration increasing, the dislocation strengthening increases simultaneously, which is closely correlated with more dislocations that are stored in high Ti-bearing Cu–Cr–Zr alloy during cold deformation.

(3) Based on thermodynamic calculations, it is found that the nucleation energy barrier for FCC-Cr is much lower than that for β'-Cu$_4$Ti or BCC-Cr, indicating that the fine FCC-Cr precipitate plays a major role in precipitation strengthening. And the increase of Ti content can reduce the FCC-Cr nucleation energy barrier to a certain extent and promote FCC-Cr nucleation in Cu–Cr–Zr–Ti alloy. Moreover, based on kinetic calculations, the increase of Ti content can increase the activation energy of the precipitation growth process of alloys, hence hindering the growth of precipitate.

Declaration of Competing Interest

The authors (*Chenying Shi, Muzhi Ma, Biaobiao Yang, Yuling Liu, Yushen Huang and Yong Du*) declare that there is no conflict of interests for the article entitled "Effect of Ti additions on microstructure and mechanical properties of Cu-Cr-Zr alloy", we do not have any possible conflicts of interest.

Supplementary materials

Supplementary material associated with this article can be found, in the online version, at doi:10.1016/j.jmst.2023.04.012.

References

[1] F.X. Huang, J.S. Ma, H.L. Ning, Y.W. Cao, Z.T. Geng, Scr. Mater. 48 (2003) 97–102.
[2] P. Fenici, D.J. Boerman, G.P. Tartaglia, J.D. Elen, J. Nucl. Mater. 212 (1994) 399–403.
[3] P.K.C. Kanigalpula, D.K. Pratihar, M.N. Jha, J. Derose, A.V. Bapat, A.R. Pal, Int. J. Adv. Manuf. Technol. 85 (2016) 711–726.
[4] X.B. Chen, F. Jiang, J.Y. Jiang, P. Xu, M.M. Tong, Z.Q. Tang, Metals (Basel) 8 (2018) 227.
[5] I.S. Batra, G.K. Dey, U.D. Kulkarni, S. Banerjee, Mater. Sci. Eng. A 356 (2003) 32–36.
[6] A. Morozova, R. Mishnev, A. Belyakov, R. Kaibyshev, Rev. Adv. Mater. Sci. 54 (2018) 56–92.
[7] K. Abib, H. Azzeddine, B. Alili, L. Litynska-Dobrzynska, A. Helbert, T. Baudin, P. Jegou, M. Mathon, P. Zieba, D. Bradai, Kov. Mater. 57 (2019) 121–129.
[8] J.H. Yuan, L.K. Gong, W.Q. Zhang, B. Zhang, H.G. Wei, X.P. Xiao, H. Wang, B. Yang, J. Mater. Res. Technol. 8 (2019) 1964–1970.
[9] N.D. Stepanov, A.V. Kuznetsov, G.A. Salishchev, G.I. Raab, R.Z. Valiev, Mater. Sci. Eng. A 554 (2012) 105–115.
[10] Y. Yang, L. Wang, L. Snead, S.J. Zinkle, Mater. Des. 156 (2018) 370–380.
[11] Y. Zhan, Y. Xu, Z. Yu, Y. Wang, H. Xie, X. Shi, Powder Metall. 49 (2006) 253–257.
[12] W.Y. Wang, J.J. Zhu, N.N. Qin, Y.F. Zhang, S.Y. Li, Z. Xiao, Q. Lei, Z. Li, J. Alloys Compd. 847 (2020) 155762.
[13] A. Meng, J.F. Nie, K. Wei, H.J. Kang, Z.J. Liu, Y.H. Zhao, Vacuum 167 (2019) 329–335.
[14] H.F. Xie, X.J. Mi, G.J. Huang, B.D. Gao, X.Q. Yin, Y.F. Li, Rare Met. 30 (2011) 650–656.
[15] H.D. Fu, S. Xu, W. Li, J.X. Xie, H.B. Zhao, Z.J. Pan, Mater. Sci. Eng. A 700 (2017) 107–115.
[16] A. Sarkar, S.V.S. Murty, M.J.N.V. Prasad, Metall. Mater. Trans. A 51 (2020) 4742–4752.
[17] S.C. Krishna, N.K. Karthick, G. Sudarshan Rao, A.K. Jha, B. Pant, R.M. Cherian, J. Mater. Eng. Perform. 27 (2018) 787–793.
[18] S.C. Krishna, K.V. Radhika, K.T. Tharian, M. Swathi Kiranmayee, G. Sudarshan Rao, A.K. Jha, B. Pant, J. Mater. Eng. Perform. 22 (2013) 2331–2336.
[19] S.C. Krishna, K.V. Radhika, K. Thomas Tharian, G. Sudarshan Rao, M. Swathi Kiranmayee, B. Pant, Mater. Sci. Forum 710 (2012) 626–631.
[20] S.C. Krishna, G.S. Rao, A.K. Jha, B. Pant, P.V. Venkitakrishnan, Mater. Sci. Eng. A 674 (2016) 164–170.
[21] S.C. Krishna, N.K. Karthick, G.M. Karthik, R. Damodaram, A.K. Jha, B. Pant, R.M. Cherian, Metallogr. Microstruct. Anal. 7 (2018) 703–710.
[22] R.R. Kumar, A. Singh, A.K. Pande, D. Tripathy, M. Amruth, T. Tharian, P.V. Venkitakrishnan, Mater. Sci. Forum 830 (2015) 362–366.
[23] S.C. Krishna, G.S. Rao, A.K. Jha, B. Pant, K.M. George, J. Mater. Eng. Perform. 24 (2015) 2341–2345.
[24] G.S. Rao, V.M.J. Sharma, S.G.S. Raman, M. Amruth, P.R. Narayanan, S.C. Sharma, P.V. VenkitaKrishnan, Mater. Sci. Eng. A 668 (2016) 97–104.
[25] H. Wang, L.K. Gong, J.F. Liao, H.M. Chen, W.B. Xie, B. Yang, J. Alloys Compd. 749 (2018) 140–145.
[26] S. Nagarjuna, K. Balasubramanian, D.S. Sarma, Mater. Sci. Eng. A 225 (1997) 118–124.
[27] S. Semboshi, Y. Kaneno, T. Takasugi, S.Z. Han, N. Masahashi, Metall. Mater. Trans. A 50 (2019) 1389–1396.
[28] E. Lee, S. Han, K. Euh, S. Lim, S. Kim, Met. Mater. Int. 17 (2011) 569–576.
[29] T.S. Thomas, A.K. Asraff, S. Sam, in: Proceedings of the National Seminar on 'Aerospace Structures Technologies-Progress & Outlook' ASET-2014, Thiruvananthapuram, 2014.
[30] D. Hull, Fractography: observing, Measuring and Interpreting Fracture Surface Topography, Cambridge University Press, UK, 1999.
[31] B.B. Guo, W.Z. Zhang, S.G. Li, X.S. Wang, Mater. Sci. Eng. A 700 (2017) 397–405.
[32] W.B. Qin, J.S. Li, Y.Y. Liu, J.J. Kang, L.N. Zhu, D.F. Shu, P. Peng, D.S. She, D.Z. Meng, Y.S. Li, Mater. Lett. 254 (2019) 116–119.
[33] T. Sakai, A. Belyakov, R. Kaibyshev, H. Miura, J.J. Jonas, Prog. Mater. Sci. 60 (2014) 130–207.
[34] J.B. Liu, M.L. Hou, H.Y. Yang, H.B. Xie, C. Yang, J.D. Zhang, Q. Feng, L.T. Wang, L. Meng, H.T. Wang, J. Alloys Compd. 765 (2018) 560–568.

[35] S. Wang, T.T. Zheng, M. Xie, Y.T. Chen, J.M. Zhang, Sci. Eng. Compos. Mater. 23 (2016) 599–603.

[36] L.F. Zou, C.M. Yang, Y.K. Lei, D. Zakharov, J.M.K. Wiezorek, D. Su, Q.Y. Yin, J. Li, Z.Y. Liu, E.A. Stach, J.C. Yang, L. Qi, G.F. Wang, G.W. Zhou, Nat. Mater. 17 (2018) 56–63.

[37] S.L. Fu, P. Liu, X.H. Chen, H.L. Zhou, F.C. Ma, W. Li, K. Zhang, Mater. Sci. Eng. A 802 (2021) 140598.

[38] S. Nagarjuna, K. Balasubramanian, D.S. Sarma, J. Mater. Sci. 34 (1999) 2929–2942.

[39] L. Huang, Z.S. Cui, X.P. Meng, X.W. Zhang, X.Y. Zhang, X.P. Song, N. Tang, Z. Xiao, Q. Lei, Z. Li, Mater. Sci. Eng. A 823 (2021) 141581.

[40] J.Z. Huang, Z. Xiao, J. Dai, Z. Li, H.Y. Jiang, W. Wang, X.X. Zhang, Mater. Sci. Eng. A 744 (2019) 754–763.

[41] G.I. Taylor, Proc. R. Soc. Lond. A 145 (1934) 362–387.

[42] H.J. Bunge, Krist. Technol. 5 (1970) 145–175.

[43] M.A. Meyers, K.K. Chawla, Mechanical Behavior of Materials, Cambridge University Press, UK, 2008.

[44] X.L. Guo, Z. Xiao, W.T. Qiu, Z. Li, Z.Q. Zhao, X. Wang, Y.B. Jiang, Mater. Sci. Eng. A 749 (2019) 281–290.

[45] D. Hull, D.J. Bacon, Introduction to Dislocations, Butterworth-Heinemann Press, Netherlands, 2001.

[46] G.K. Williamson, W.H. Hall, Acta Metall. 1 (1953) 22–31.

[47] T.H. Courtney, Mechanical Behavior of Materials, Waveland Press, USA, 2005.

[48] J.B. Correia, H.A. Davies, C.M. Sellars, Acta Mater. 45 (1997) 177–190.

[49] J.Y. Zhang, S. Lei, Y. Liu, J.J. Niu, Y. Chen, G. Liu, X. Zhang, J. Sun, Acta Mater. 60 (2012) 1610–1622.

[50] S. Nagarjuna, M. Srinivas, K. Balasubramanian, D.S. Sarma, Mater. Sci. Eng. A 259 (1999) 34–42.

[51] Y.L. Liu, P. Zhou, S.H. Liu, Y. Du, Calphad 59 (2017) 1–11.

[52] R. Arroyave, T.W. Eagar, L. Kaufman, J. Alloys Compd. 351 (2003) 158–170.

[53] O. Redlich, A. Kister, J. Ind. Eng. Chem. 40 (1948) 345–348.

[54] Y.M. Muggianu, M. Gambino, J.P. Bros, J. Chim. Phys. Phys.-Chim. Biol. 72 (1975) 83–88.

[55] E. Hall, Proc. R. Soc. B 64 (1951) 747.

[56] N. Petch, J. Iron Steel Inst. 174 (1953) 25–28.

[57] Y. Liu, Z. Li, Y.X. Jiang, Y. Zhang, Z.Y. Zhou, Q. Lei, J. Mater. Res. 32 (2017) 1324–1332.

[58] H. Abrams, Metallography 4 (1971) 59–78.

[59] B. Holmedal, Philos. Mag. Lett. 95 (2015) 594–601.

[60] D.D. Zhao, Y.J. Xu, S. Gouttebroze, J. Friis, Y.J. Li, Metall. Mater. Trans. A 51 (2020) 4838–4852.

[61] H.C. Peng, W.B. Xie, H.M. Chen, H. Wang, B. Yang, J. Alloys Compd. 852 (2021) 157004.

[62] A. Bodyakova, R. Mishnev, A. Belyakov, R. Kaibyshev, J. Mater. Sci. 57 (2022) 13043–13059.

[63] W. Tian, L.M. Bi, F.C. Ma, J.D. Du, Vacuum 149 (2018) 238–247.

[64] D. Kashchiev, Nucleation, Elsevier, (2000).

[65] J.W. Christian, The Theory of Transformations in Metals and Alloys, Newnes Press, Netherlands, 2002.

[66] A. Chbihi, X. Sauvage, D. Blavette, Acta Mater. 60 (2012) 4575–4585.

[67] S. Chen, Y.H. Duan, B. Huang, W.C. Hu, Philos. Mag. 95 (2015) 3535–3553.

[68] Q. Lei, Z. Li, A.Y. Zhu, W.T. Qiu, S.Q. Liang, Mater. Charact. 62 (2011) 904–911.

[69] F. Hernandez-Santiago, V.M. Lopez-Hirata, P.E. Hernandez-Duran, M.L. Sauce-do-Muñoz, E.O. Avila-Davila, in: TMS 2017 146th Annual Meeting & Exhibition Supplemental Proceedings, Springer, Cham, Switzerland, 2017.

[70] C. Aguilar, V.D.P. Martinez, J.M. Palacios, S. Ordoñez, O. Pavez, Scr. Mater. 57 (2007) 213–216.

[71] J. Miyake, M.E. Fine, Acta Metall. Mater. 40 (1992) 733–741.

[72] R.W. Cahn, P. Haasen, Physical Metallurgy, Elsevier Press, Netherlands, 1996.

[73] K. Zhang, J.J. Yang, J. Li, X.H. Chen, H.L. Zhou, P. Liu, J. Alloys Compd. 851 (2021) 156776.

[74] Z.K. Huang, R.H. Shi, X.Y. Xiao, H.D. Fu, Q. Chen, J.X. Xie, Mater. Today Commun. 27 (2021) 102378.